Photonic quantum simulations of coupled $\mathcal{PT}$-symmetric Hamiltonians

Nicola Maraviglia[1], Patrick Yard,[1] Ross Wakefield,[1] Jacques Carolan,[2] Chris Sparrow,[1,3]
Levon Chakhmakhchyan[1,*], Chris Harrold,[1] Toshikazu Hashimoto,[4] Nobuyuki Matsuda[5,†]
Andrew K. Harter,[6] Yogesh N. Joglekar[6,‡] and Anthony Laing[1,§]

[1]*Quantum Engineering Technology Labs, H. H. Wills Physics Laboratory and Department of Electrical and Electronic Engineering,
University of Bristol, Bristol BS8 1FD, United Kingdom*
[2]*Center for Hybrid Quantum Networks (Hy-Q), Niels Bohr Institute,
University of Copenhagen, Blegdamsvej 17, DK-2100 Copenhagen, Denmark*
[3]*Department of Physics, Imperial College London, London SW7 2AZ, United Kingdom*
[4]*NTT Device Technology Laboratories, NTT Corporation, Atsugi, Kanagawa 243-0198, Japan*
[5]*NTT Basic Research Laboratories, NTT Corporation, Atsugi, Kanagawa 243-0198, Japan*
[6]*Department of Physics, Indiana University–Purdue University Indianapolis (IUPUI), Indianapolis, Indiana 46202, USA*

Parity-time-symmetric ($\mathcal{PT}$-symmetric) Hamiltonians are generally non-Hermitian and give rise to exotic behavior in quantum systems at exceptional points, where eigenvectors coalesce. The recent realization of $\mathcal{PT}$-symmetric Hamiltonians in quantum systems has ignited efforts to simulate and investigate many-particle quantum systems across exceptional points. Here, we use a programmable integrated photonic chip to simulate a model composed of twin pairs of $\mathcal{PT}$-symmetric Hamiltonians, with each the time reverse of its twin. We simulate quantum dynamics across exceptional points including two- and three-particle interference, and a particle-trembling behavior that arises due to interference between subsystems undergoing time-reversed evolutions. These results show how programmable quantum simulators can be used to investigate foundational questions in quantum mechanics.

I. INTRODUCTION

Dirac Hermiticity of a Hamiltonian has been a tenet of quantum theory since its inception. This constraint guarantees real eigenvalues, orthogonal eigenstates, and a unitary time evolution; it reflects the dynamics of an isolated system. Over the past two decades, non-Hermitian Hamiltonians that are symmetric under combined parity ($\mathcal{P}$) and time-reversal ($\mathcal{T}$) transformations were extensively investigated, first mathematically [1,2] and then experimentally in classical wave systems [3,4]. In the classical domain, $\mathcal{PT}$-symmetric systems have shown remarkable properties such as unidirectional invisibility [5], single-mode [6,7] and topological [8,9] lasing, topological energy transfer [10], mode switching [11], and enhanced sensitivity [12,13]. While generally non-Hermitian, $\mathcal{PT}$-symmetric Hamiltonians exhibit exceptional points (EPs) at which two (or more) eigenvalues become degenerate and

the corresponding eigenstates coalesce. For all these advances, the role of thermal and quantum noise on EPs in these semiclassical systems is not yet understood [14,15].

Realizing $\mathcal{PT}$-symmetric systems in the quantum domain has been a major challenge [16], and its circumvention has relied on two methods. The first approach, known as passive $\mathcal{PT}$ symmetry, is based on the equivalence (after normalization) of a $\mathcal{PT}$-symmetric Hamiltonian and a dissipative Hamiltonian with mode-selective losses [17,18]. Such a dissipative Hamiltonian arises naturally from a Lindblad approach for open quantum systems when certain quantum jumps are ignored and allows the implementation of coherent, nonunitary dynamics in a minimal quantum system [19]. The second method uses Hamiltonian dilation that places the $\mathcal{PT}$-symmetric Hamiltonian in a larger Hilbert space by introducing an ancillary two-level system [20–22], and the coherent, nonunitary dynamics of interest are recovered from the unitary dynamics in the larger Hilbert space. In the first approach, the evolution time of the system is limited by the exponentially decaying signal or postselection success probability, while the second method requires a time-dependent Hermitian Hamiltonian for the larger Hilbert space.

Here, we propose a framework for the quantum simulation of $\mathcal{PT}$-symmetric Hamiltonians that is particularly suited to technology platforms that allow the direct implementation of unitary transformations [23–25]. The nonunitary evolution operator, and a second operator that is the time reverse of the first, are embedded together into a global unitary transformation that is then implemented by the device. The

---

*Present address: Krisp, Hrachya Kochar 5/1, Yerevan 0033, Armenia.

†Present address: Department of Communications Engineering, Graduate School of Engineering, Tohoku University, Sendai, Japan.

‡yojoglek@iupui.edu

§anthony.laing@bristol.ac.uk

overall evolution in this model allows single- or many-particle excitations to tunnel between the twin systems, with a probability that scales with the non-Hermiticity of the simulated Hamiltonians. This construction permits the experimental investigation of states superposed across opposite directions of time in the context of non-Hermitian Hamiltonians.

We experimentally simulate multiparticle dynamics [26] in two- and three-mode $\mathcal{PT}$-symmetric Hamiltonians using a programmable photonic chip [27] and ensembles of one-, two-, and three-photon input states. We reproduce the dynamics in the $\mathcal{PT}$-symmetric regime (defined by real eigenvalues) and across the EP into the $\mathcal{PT}$-symmetry-broken regime (defined by complex-conjugate eigenvalues), including the effects of mutual coherence and interference between the forward-in-time and backward-in-time subsystems. Combined with the current advances in photonic technologies, these demonstrations point towards the inclusion of non-Hermitian simulations in the realm of quantum technologies.

II. MODEL AND SIMULATION PROCEDURE

Our simulation approach begins by considering a family of $\mathcal{PT}$-symmetric systems consisting of a linear chain of N modes with a coupling amplitude $J > 0$ between nearest-neighbor modes. In addition, an imaginary potential of opposite sign $\pm i\gamma$ located in the two spatially symmetric end modes determines a gain and a loss site. We fix the energy scale of our system by choosing $J = +1$ so that the Hamiltonian reads

$$H_N(\gamma) = -\sum_{k=1}^{N-1}(|k\rangle\langle k+1| + |k+1\rangle\langle k|)$$
$$+ i\gamma(|1\rangle\langle 1| - |N\rangle\langle N|), \qquad (1)$$

where $|k\rangle$ is the state associated with the kth mode. Using $\{|k\rangle\}_{k=1}^N$ as a basis, the parity operator we choose is represented by the antidiagonal matrix $\mathcal{P}_{mn} = \delta_{m,N+1-n}$, and the time-reversal operator $\mathcal{T}$ corresponds to the complex-conjugation operation. $H_N(\gamma)$ presents an EP for a critical value $\gamma = \gamma_c$ that depends on N [28,29]. The spectrum of the Hamiltonian $H_N(\gamma)$ is purely real for $\gamma < \gamma_c$, and the corresponding eigenvectors are simultaneous eigenvectors of the antilinear $\mathcal{PT}$ operator (unbroken symmetry phase). At the EP, $\gamma = \gamma_c$, two or more states coalesce, while at $\gamma > \gamma_c$, two eigenstates with opposite imaginary eigenvalue emerge from the previously coalescing states (broken symmetry phase). The full spectrum of the Hamiltonian can be obtained by solving a set of transcendental equations reported in Ref. [28], but γ_c is given by a simple closed form: $\gamma_c/J = 1$ whenever N is even and $\gamma_c/J = \sqrt{(N+1)/(N-1)}$ when N is odd. For a static, non-Hermitian Hamiltonian $H_N(\gamma)$, the nonunitary time evolution operator $G_N(\gamma, t)$ is given by (assuming $\hbar = 1$)

$$G_N(\gamma, t) = \exp[-iH_N(\gamma)t]. \qquad (2)$$

We note that these choices set the time scale for our system, $\hbar/J$, to unity.

To simulate its dynamical evolution with a device that implements unitary transformations, we adopt the Halmos unitary dilation [30,31]. Namely, we first rescale $G_N(\gamma, t)$ by

its largest singular value $||G_N(\gamma, t)||_2$ obtaining

$$\tilde{G}_N(\gamma, t) := G_N(\gamma, t)/||G_N(\gamma, t)||_2, \qquad (3)$$

so that the operator norm of the scaled operator $\tilde{G}_N(\gamma, t)$ is unity. Then, defining the defect operator as

$$D_N(\tilde{G}_N) := [\mathbb{1} - \tilde{G}_N(\gamma, t)\tilde{G}_N^\dagger(\gamma, t)]^{1/2}, \qquad (4)$$

we construct the following unitary transformation $U_{2N}(\gamma, t)$ defined on a Hilbert space twice the size. The block matrix representation of $U_{2N}(\gamma, t)$ is

$$U_{2N}(\gamma, t) = \begin{bmatrix} \tilde{G}_N(\gamma, t) & iD_N(\tilde{G}_N) \\ iD_N(\tilde{G}_N^\dagger) & \tilde{G}_N^\dagger(\gamma, t) \end{bmatrix}. \qquad (5)$$

We map the modes of the dilated Hilbert space onto the spatial modes of a reprogrammable linear optical chip. The time evolution of excitations in the $\mathcal{PT}$-symmetric system is simulated by injecting single photons into the optical circuit and reprogramming it to implement the unitary transfer matrix $U_{2N}(\gamma, t)$ for a sequence of time steps $\{U_{2N}(\gamma, t_i)\}_i$; see Fig. 1. To simulate the evolution determined by $H_N(\gamma)$, we encode the initial state in the first N modes of the interferometer and consider detection events on the outputs of those same modes. Our construction is applicable for $\mathcal{PT}$-symmetric systems even when the spectrum of the Hamiltonian becomes complex, allowing simulations across exceptional points. We also emphasize that since we realize the unitary, and not the (dilated) Hamiltonian, time is a parameter and so we can simulate arbitrary time scales. Specifically, we can simulate the long-time dynamics expected at the EP, due to the vanishing eigenvalue gap.

Interestingly, since the Hamiltonian is transpose-symmetric, i.e., $H_N^\dagger(\gamma) = H_N^*(\gamma)$, the global unitary $U_{2N}(\gamma, t)$ describes two coupled $\mathcal{PT}$-symmetric systems that are the time reverse of each other. Indeed, $\tilde{G}_N^\dagger(\gamma, t) = \tilde{G}_N^*(\gamma, t) = \mathcal{T}\tilde{G}_N(\gamma, t)\mathcal{T}^{-1}$, meaning that a system initialized in the last N modes of the interferometer transforms with a backwards-in-time (reverse) evolution. Whenever $\gamma \neq 0$, the two systems are coupled by the defect matrix D_N, and excitations can tunnel between these two systems. In addition to simulating individual $\mathcal{PT}$ systems, the statistics output from the photonic chip track the unitary evolution of the closed composite system.

We also note that the above dilation process is not specific to $\mathcal{PT}$ Hamiltonians. Any nonunitary evolution operator, $G_N(t)$, can be embedded in a larger unitary transformation, following the above method. This process has already been used to simulate Lindbladian dynamics [32] and could be extended to simulate anti-$\mathcal{PT}$ systems [33].

III. EXPERIMENTAL PROCEDURE

Our photonic chip comprises a triangular mesh of 15 interconnected Mach-Zehnder interferometers, controlled by 30 metallic thermo-optic phase shifters, and is capable of implementing any unitary linear optical transformation over its six waveguides (see Ref. [27] for additional device details). By means of the algorithm demonstrated by Reck *et al.* for the decomposition of any discrete optical unitary operator [34], for each $U_{2N}(\gamma, t_i)$ we retrieve the list of phases which, when applied in our interferometer, implement the desired unitary
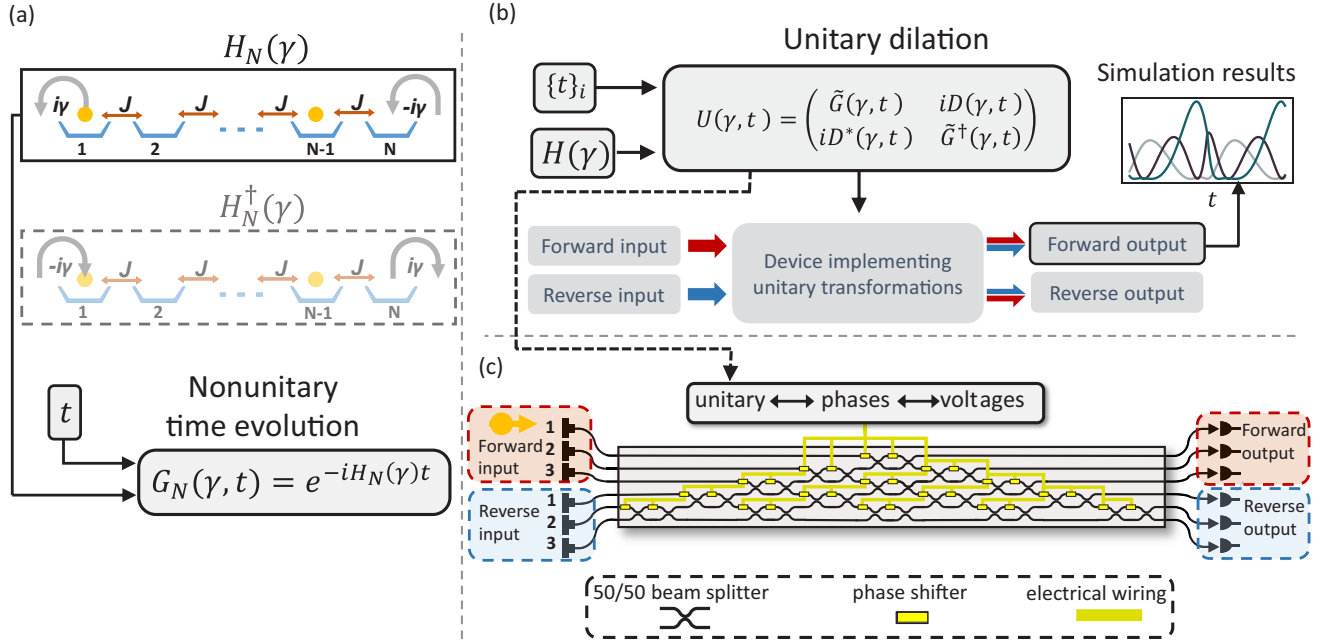
FIG. 1. (a) Graphical representation of the simulated $\mathcal{PT}$-symmetric non-Hermitian Hamiltonian $H_N(\gamma)$ that describes an open quantum system. Excitations, represented by yellow circles, can populate the N modes of a linear chain. Nearest-neighbor modes are coupled by a potential J that is set to unity during the simulations reported in this paper. The imaginary potential, $\pm i\gamma$, has the effect of amplifying and deamplifying the probability amplitude of an excitation in the first and last mode, respectively. $H_N^\dagger(\gamma)$ is equivalent to $H_N(\gamma)$ with the first and last modes swapped. The time evolution of a system with Hamiltonian $H_N(\gamma)$ is described by a nonunitary operator $G_N(\gamma, t)$. (b) Simulation procedure based on unitary dilation. Given a non-Hermitian Hamiltonian $H(\gamma)$ and an evolution time t, it is possible to create a unitary $U(\gamma, t)$ that consists of $\tilde{G}(\gamma, t) = G(\gamma, t)/||G(\gamma, t)||$ and an auxiliary matrix $D(\gamma, t)$. The simulation proceeds by implementing $U(\gamma, t)$ and initializing a desired input state in modes of the device corresponding to the forward system input. The effect of the unitary device will transform the input and distribute it across the forward and reverse output modes. When the output state is detected in the forward output, the input state successfully transforms via $\tilde{G}(\gamma, t)$. (c) Photonic implementation of the quantum simulation. Single-photon states are injected into the input ports of the first $N = 3$ waveguides of a configurable integrated photonic circuit. Forward and reverse output are detected at the first and last output ports of the interferometer. A triangular mesh of integrated beam splitters and metallic phase shifters allows us to reconfigure the integrated interferometer to implement the desired $U(\gamma, t)$.

transformation. Calibration of the on-chip thermo-optic phase shifters allows us to map a desired phase shift to a voltage bias to be set. Input photons are generated with a bulk spontaneous parametric downconversion source and coupled in and out of the chip with packaged optical fibers, before detection with silicon avalanche photodiodes. This setup is capable of simulating coupled $\mathcal{PT}$-symmetric Hamiltonians with $N = 2$ and $N = 3$ modes in each subsystem and multiparticle evolution.

Tuning the strength of the complex potential γ corresponds to changing the unitary matrix $U_{2N}(\gamma, t_i)$, and therefore the set of phases dialed on our chip. In this way, all values of γ can be implemented in the same way, allowing us to investigate the system dynamics in four regimes: uncoupled Hermitian evolution, coupled $\mathcal{PT}$-symmetric evolution, evolution at the EP, and evolution in the broken symmetry phase. As we increase γ, we also increase the coupling between the systems, $iD(\gamma, t)$, which correspondingly decreases the probability of a photon remaining in the desired subsystem.

To distinguish between the state of the simulated system and the photonic Fock state of our simulator, we will use the subscript p for the latter. That is, for $N = 2$, Fock states $\{|1_p 0_p\rangle, |0_p 1_p\rangle\}$ encode the states $\{|1\rangle, |2\rangle\}$, respectively, while for $N = 3$, Fock states $\{|1_p 0_p 0_p\rangle, |0_p 1_p 0_p\rangle, |0_p 0_p 1_p\rangle\}$ encode the states $\{|1\rangle, |2\rangle, |3\rangle\}$. The Fock states $|0_p 0_p 0_p\rangle$

or $|0_p 0_p\rangle$, corresponding to an unoccupied system, will be represented with $|\text{vac}\rangle$. Furthermore, subscript F or R will differentiate between the forward and reverse systems, or equivalently, between the first or last N modes of our interferometer, respectively.

IV. SIMULATION OF TWO-MODE $\mathcal{PT}$-SYMMETRIC SYSTEMS

We first simulate two-mode $\mathcal{PT}$-symmetric systems. With $N = 2$, the eigenvalues of the Hamiltonian are $\epsilon = \pm\sqrt{1 - \gamma^2}$. Since the global model in this instance comprises four modes in total, there is sufficient redundancy in the six-mode chip to implement a separate tomography stage. The first section of the chip implements the state evolution described by $\{U_4(\gamma, t_i)\}_i$. The remaining part of the chip is used to perform projective measurements allowing the reconstruction of the density matrices for evolved single-photon states.

Figure 2 shows the results from the simulations of the unbroken and broken symmetry phases. Experimental points are presented next to theory lines. In Figs. 2(a) and 2(b) we report the probability for an excitation initialized in the state $|1\rangle_F \otimes |\text{vac}\rangle_R$ to be detected in any of the forward system
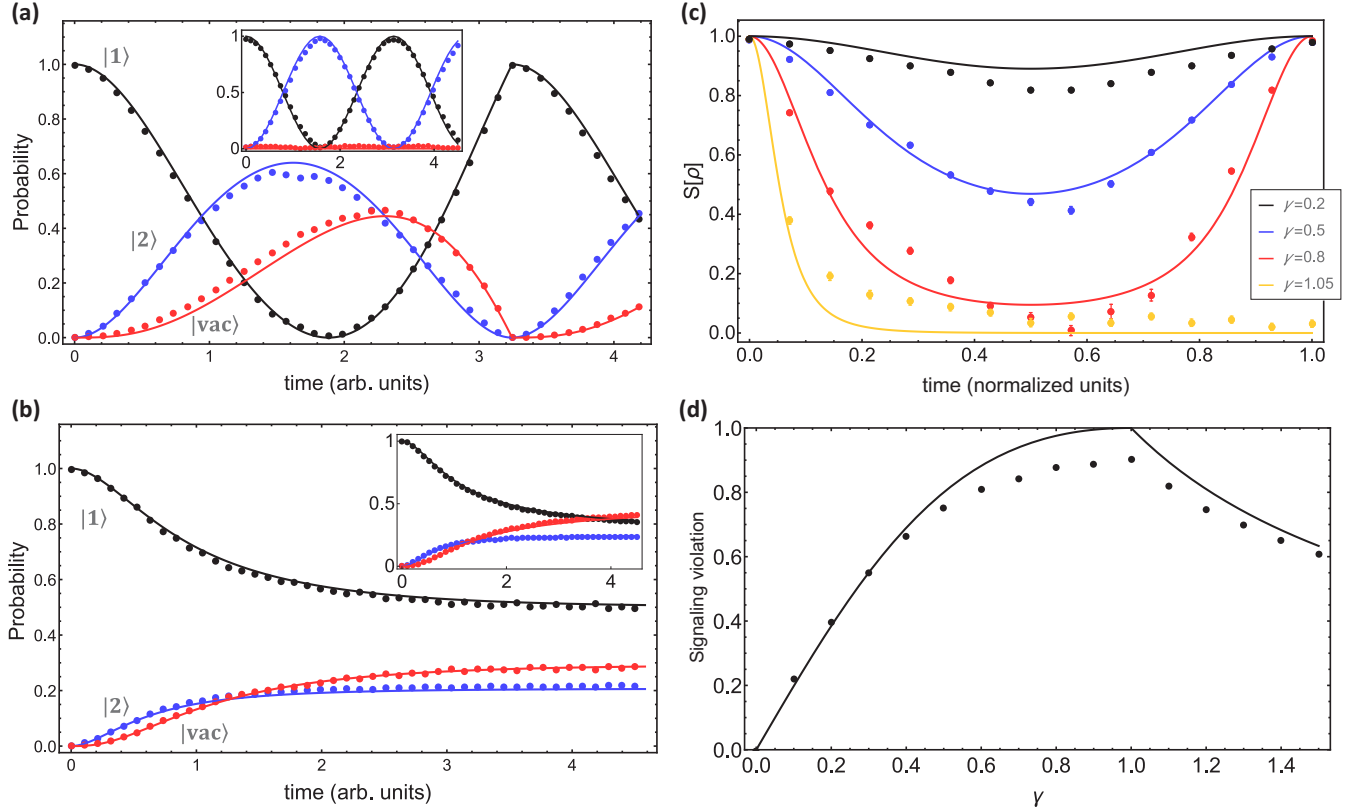
FIG. 2. Simulation of the forward system across different regimes of the $\mathcal{PT}$ Hamiltonian. Solid lines (dots) correspond to the theory (experimental data). (a) and (b) A single excitation is initialized in $|1\rangle_F$ and observed in the $\{|vac\rangle, |1\rangle, |2\rangle\}_F$ basis as shown with red, black, and blue data, respectively. (a) In the unbroken symmetry phase ($\gamma = 0.25$), the plot shows the tunneling of excitations between the forward and reverse systems resulting in a periodic oscillation in the vacuum probability; the inset shows the Hermitian regime ($\gamma = 0$) with a constant vacuum probability of 0 and sinusoidal oscillations between the two populated levels. (b) In the broken symmetry phase ($\gamma = 1.1$), the evolution is not periodic, and the system tends rapidly to a steady state; the inset shows the evolution of the system at the exceptional point. (c) and (d) Evolution of the initial state $\rho_0 = 0.5|1\rangle_F\langle 1|_F + 0.5|2\rangle_F\langle 2|_F$. (c) The entropy of the system is periodic for $\gamma < 1$ and goes asymptotically to 0 for $\gamma > 1$. Time is reported in units normalized as a function of γ by dividing by $\tau = \pi/\sqrt{|1 - \gamma^2|}$. (d) Signaling violation as a function of γ and for evolution time $t = \pi/\sqrt{|1 - \gamma^2|}$ with a maximum at the exceptional point $\gamma = 1$. The outcomes of measurements on one qubit are affected by local operations on a $\mathcal{PT}$ qubit, entangled with the first.

modes, but we enforce that the cumulative outcome statistic from the forward and reverse subsystems is normalized to 1. To do so, we retained both the events where the propagating excitation was detected in the forward subsystem modes heralding its evolution according to $\tilde{G}$, and those where the excitation has left the forward modes to reappear in the reverse subsystem modes. If the excitation moves to the reverse system, the forward system is left in its vacuum state with no excitation, $|vac\rangle_F$, and as such is reported in Figs. 2(a) and 2(b). A formal derivation of the forward state description as a result of a partial trace over the modes of the reverse system is available in Appendix C. In the unbroken symmetry phase, shown in Fig. 2(a) with $\gamma = 0.25$, the time evolution of the system is periodic, and the finite probability of detecting $|vac\rangle_F$ indicates that the excitation can tunnel from the forward system to its time-reversed twin. In contrast, the inset in the same plot shows the evolution when $\gamma = 0$. Since the system is closed and Hermitian, only sinusoidal oscillations of the probabilities of detecting $|1\rangle_F$ and $|2\rangle_F$ are observed. Figure 2(b) shows, instead, the evolution in the

broken symmetry phase with $\gamma = 1.1$. The system rapidly tends to a steady state with no oscillations and with a nonzero probability of finding the excitation in either the forward or reverse systems. Such a qualitative distinction between the two regimes is caused by the characteristic phase transition at the EP. In the inset of Fig. 2(b), we report the evolution observed at the EP when $\gamma = 1$. Here, the period of the system oscillation $\tau = \pi/\sqrt{1 - \gamma^2}$ tends to infinity. The probabilities evolve towards a never-reached turning point, and the systems effectively tends to a steady state with coefficients that follows a polynomial power law. In contrast, in the broken symmetry phase, the system approaches its steady state with an exponential power law whose characteristic time, $\tau' = \pi/\sqrt{\gamma^2 - 1}$, decreases for increasing γ.

Figures 2(c) and 2(d) show the evolution of a completely mixed input state, $\rho_0 = 0.5|1\rangle_F\langle 1|_F + 0.5|2\rangle_F\langle 2|_F$, which was realized by first entangling two photons using a photonic gate [35]. The total unitary implemented by the chip is obtained by multiplying together the transfer matrix that describes the entangling gate, and $U_4(\gamma, t)$, in such a way that one photon is

injected into the two modes of the forward system of $U_4(\gamma, t)$ while the second photon of the entangled pair is transmitted by two ancillary waveguides not affected by the $U_4(\gamma, t)$. To herald the successful generation of the entangled photon pair, the tomographic reconstruction of the state is performed by retaining only the coincidental events of a photon detected in the forward $\mathcal{PT}$-symmetric system and a photon detected in the two ancillary waveguides.

In Fig. 2(c) we report the evolution of the von Neumann entropy $S[\rho(t)]$, of the initially mixed $\mathcal{PT}$ qubit ρ_0, for different values of γ. As opposed to a closed Hermitian system whose entropy is a constant of motion, in the unbroken symmetry phase, the entropy is a nonmonotonic function of time. By reporting the time parameter in units of $\tau = \pi/\sqrt{|1 - \gamma^2|}$, the entropy has a minimum when $t = 0.5\tau$. Instead, when $\gamma > \gamma_c$, the entropy decays to 0. The periodic behavior of the entropy in the $\mathcal{PT}$-symmetric phase indicates the flow of information from the forward system to its time-reversed twin and back [36].

Figure 2(d) shows the results of a signaling violation test, as described in Refs. [37,38]. The test refers to the possibility of affecting the state of a system B by performing only local operations on a system A. For a pair of qubits, the signaling violation, $s.v.$, expressed in terms of the measurement probability P on the qubit B, reads

$$s.v. = [\text{P}(1|S) - \text{P}(2|S)] - [\text{P}(1|I) - \text{P}(2|I)], \quad (6)$$

where 1 (2) corresponds to the first (second) level of the qubit B, and I (S) refers to a local identity (swap) transformation applied to the qubit A. Our simulation proceeds by entangling the qubits A and B, then applying either the identity or the swap transformation, and finally simulating the evolution of qubit A with the $\mathcal{PT}$-symmetric Hamiltonian. Meanwhile, the qubit B is encoded by the photon transmitted over the two ancillary waveguides. Figure 2(d) shows that the probabilities of the two alternative outputs for qubit B are conditioned by the a local unitary transformation applied to the $\mathcal{PT}$ qubit A prior to its nonunitary evolution. The no-signaling condition is violated for all $\gamma \neq 0$ and is maximal for $\gamma = \gamma_c$. To maximize the signaling violation, the evolution time for the $\mathcal{PT}$ system is set to $t = \pi/\sqrt{|1 - \gamma^2|}$.

Since in our framework excitations initialized in one system naturally tunnel to its time-reversed twin, we investigate the interference effects that arise from an initial excitation coherently superposed across the forward and the reverse systems. Interference between systems evolving in opposite directions in time is an effect pertinent to the foundations of quantum mechanics [39] and gives rise to peculiar quantum effects predicted in the dynamics of a relativistic electron [40,41], recently investigated with trapped ions and Bose-Einstein condensates [42,43].

We choose to measure an observable that manifests a qualitative change depending both on the coherence between the two systems and their deviation from Hermiticity. We define a generalization of the σ_x operator for the forward (reverse) system

$$S_{\text{F(R)}} = \begin{pmatrix} 0 & 0 & 0 \\ 0 & 0 & 1 \\ 0 & 1 & 0 \end{pmatrix}, \quad (7)$$

as represented in the $\{|\text{vac}\rangle_{\text{F(R)}}, |1\rangle_{\text{F(R)}}, |2\rangle_{\text{F(R)}}\}$ basis. Such an observable is a constant of motion in the Hermitian regime and can be considered as a discrete-variable equivalent of a particle coordinate operator [44]. However, if we prepare an input state that is a coherent superposition of the forward and reverse subsystems, such as $(|1\rangle_{\text{F}} + |1\rangle_{\text{R}})/\sqrt{2}$, both $\langle S_{\text{F}} \rangle$ and $\langle S_{\text{R}} \rangle$ exhibit oscillatory behavior.

The amplitude of these oscillations is reduced if the coherence between the states $|1\rangle_{\text{F}}$ and $|1\rangle_{\text{R}}$ decreases, and it vanishes if the input is a statistical mixture of $|1\rangle_{\text{F}}$ and $|1\rangle_{\text{R}}$ [Fig. 3(a)]. We therefore associate this oscillatory behavior with the coherent interference between forward and reverse modes of the $\mathcal{PT}$-symmetric doublet, a situation that is analogous to the *Zitterbewegung* effect [40]. This predicts an oscillatory or "trembling" behavior of the position expectation value for a relativistic electron, stemming from interference between positive and negative energy solutions of the Dirac equation. For this experiment, the mixed state spread across the forward and reverse system is simulated by statistically averaging the results from two orthogonal pure single-particle input states. We finally note that in the broken symmetry phase [Fig. 3(b)], $\langle S_{\text{F(R)}} \rangle$ no longer exhibits oscillatory behavior since the system loses its periodicity, but the final configuration of the system changes greatly depending on the initial coherence between the two subsystems.

V. THREE-MODE AND MANY-PARTICLE $\mathcal{PT}$-SYMMETRIC SYSTEMS

We have up to now discussed the nonunitary evolution of a single excitation over two modes, thereby simulating single-particle $\mathcal{PT}$-symmetric systems. We now fix $N = 3$. In addition to gain and loss modes, the three-mode $\mathcal{PT}$-symmetric systems possess a neutral mode. With $N = 3$, the eigenvalues of $H_N(\gamma)$ become $\epsilon \in \{0, \sqrt{2 - \gamma^2}, -\sqrt{2 - \gamma^2}\}$. We refer the reader to Appendix F for an analysis of the evolution of a single excitation over three modes. Instead, here we show how the same interferometer set to realize the evolution described by $U_{2N}(\gamma, t)$ can be used to study the interference of many identical photons undergoing nonunitary time evolution under a $\mathcal{PT}$-symmetric Hamiltonian.

Using pairs of indistinguishable photons, we observe the evolution of the following two-particle input states:

$$|\Omega_1\rangle = |1_p 1_p 0_p\rangle_{\text{F}} \otimes |0_p 0_p 0_p\rangle_{\text{R}},$$
$$|\Omega_2\rangle = \mathcal{PT}|\Omega_1\rangle = |0_p 1_p 1_p\rangle_{\text{F}} \otimes |0_p 0_p 0_p\rangle_{\text{R}}. \quad (8)$$

$|\Omega_1\rangle$ has one photon in the gain and neutral modes each, while $|\Omega_2\rangle$ has one photon in the loss and neutral modes each. Figures 4(a)–4(c) show the probability for the system to collapse onto gain-neutral, gain-loss, and neutral-loss modes, i.e., states $|1_p 1_p 0_p\rangle_{\text{F}}$, $|1_p 0_p 1_p\rangle_{\text{F}}$, and $|0_p 1_p 1_p\rangle_{\text{F}}$, respectively, as a function of time. We choose four values of γ, in the Hermitian, $\mathcal{PT}$-symmetric ($\gamma = \sqrt{2}/2, \gamma = 3\sqrt{2}/4$), and $\mathcal{PT}$-symmetry-broken regimes ($\gamma = 1.1\sqrt{2}$). A similar procedure can be adopted to simulate the non-Hermitian two-photon (Hong-Ou-Mandel) interference [26]. The probabilities reported in Figs. 4(a)–4(c) are normalized over all the possible antibunched patterns over the six modes of the interferometer. We note that, due to the $\mathcal{PT}$ symmetry
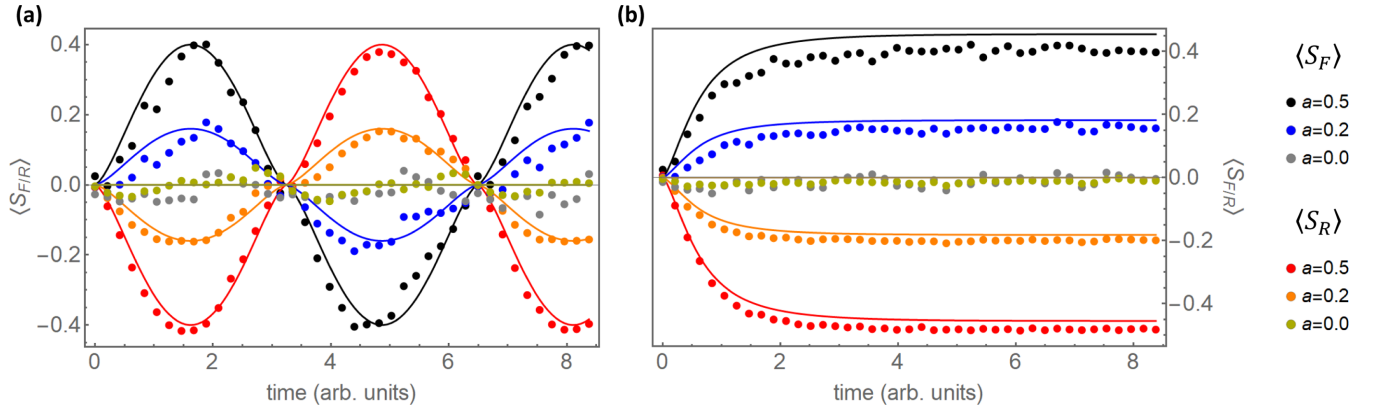
FIG. 3. Simulation of *Zitterbewegung*-like interference effects between coupled, time-reversed, two-mode $\mathcal{PT}$ systems. Expectation values of $S_{\text{F(R)}} = |1\rangle_{\text{F(R)}}\langle 2|_{\text{F(R)}} + |2\rangle_{\text{F(R)}}\langle 1|_{\text{F(R)}}$ for the system initialized as $\rho_{\text{in}} = 1/2(|1\rangle_{\text{F}}\langle 1|_{\text{F}} + |1\rangle_{\text{R}}\langle 1|_{\text{R}}) + a(|1\rangle_{\text{F}}\langle 1|_{\text{R}} + |1\rangle_{\text{R}}\langle 1|_{\text{F}})$ are shown. The parameter a characterizes the degree of coherence between the time-reversed systems. (a) In the unbroken symmetry phase ($\gamma = 0.25$), the amplitude of the oscillations of $\langle S_{\text{F(R)}}\rangle$ is proportional to the initial level of coherence of the input state. (b) In the broken symmetry phase ($\gamma = 1.1$), the initial level of coherence of the input state dictates the saturation level of $\langle S_{\text{F(R)}}\rangle$.

between these input states, we expect their evolution to proceed in opposite directions in time and to present an exchange of probabilities between the observation of the patterns $|1_p 1_p 0_p\rangle$ and $|0_p 1_p 1_p\rangle$. The probability of detecting one photon in gain and neutral modes each at time t starting from state $|\Omega_1\rangle$ is equal to the probability, at time $-t$, of detecting one photon in neutral and loss modes each when starting from state $|\Omega_2\rangle$. For these reasons, data collected for the input state $|\Omega_2\rangle$ have been plotted in the reverse temporal direction to simplify the comparison with the input state $|\Omega_1\rangle$. By increasing the value of γ, the system undergoes the transition from the symmetric to the broken symmetry phase characterized by an increase of the period of the evolution, for $\gamma < \sqrt{2}$, and by a nonperiodic evolution, for $\gamma > \sqrt{2}$.

Lastly, we demonstrate the effect of non-Hermiticity on photon bunching by starting with a maximally antibunched three-photon input state,

$$|\chi_1\rangle = |1_p 1_p 1_p\rangle_{\text{F}} \otimes |0_p 0_p 0_p\rangle_{\text{R}}. \tag{9}$$

To prepare the desired input state, we simultaneously collect two photon pairs and then use one of these photons to herald the generation of a three-photon antibunched state, which we inject into the chip. The data in Figs. 4(d)–4(f) show the evolution of the probability of different photon bunching events in the forward system modes. Due to the underlying parity-time symmetry, the probability distribution satisfies $\text{Prob}(t, |\psi\rangle) = \text{Prob}(T(\gamma) - t, \mathcal{P}|\psi\rangle)$, where $T(\gamma) = 2\pi/\sqrt{|2 - \gamma^2|}$ is the fundamental period of a $\mathcal{PT}$-symmetric trimer. Additionally, in the Hermitian limit, due to the underlying parity symmetry, the probability of two photons in mode 1 and one photon in mode 2 (i.e., pattern $|2_p, 1_p, 0_p\rangle_{\text{F}}$) is equal to that of its parity-symmetric pattern $|0_p, 1_p, 2_p\rangle_{\text{F}}$. When $\gamma > 0$, the exchange symmetry between modes 1 and 3 is broken; the weight at smaller times $t < T(\gamma)/2$ shifts to the gain mode, and the weight at times $t > T(\gamma)/2$ shifts to the loss mode. For $\gamma = 0.2$, parity-symmetric output patterns such as $|2_p 0_p 1_p\rangle_{\text{F}}$ and $|1_p 0_p 2_p\rangle_{\text{F}}$ show probability curves that are exchanged under time inversion $t \to T(\gamma) - t$.

It is computationally complex to simulate the evolution of quantum Hamiltonians [32] that produce particle statistics which are governed by intractable matrix functions. In the case of boson sampling [46], in which photons propagate in a circuit that is ideally described by a unitary matrix, classical intractability arises because the detection statistics are given by permanents of complex matrices. Yet photon loss reduces the computational complexity in experimental implementations of boson sampling [47]. Similarly, a photonic simulation of a traditional model for an open system, such as the Lindblad approach, could become classically tractable via the loss that is necessarily built into the model. However, in our simulation model for twin $\mathcal{PT}$-symmetric Hamiltonians, while each subsystem is open and lossy, the overall model is unitary and an ideal implementation is lossless; generally, statistics provide information about both the forward and backward subsystems, and the relation between them.

VI. DISCUSSION

The theory of $\mathcal{PT}$-symmetric Hamiltonians emerged two decades ago as a complex extension of quantum mechanics [48]. Over the past decade, it has galvanized research primarily in the classical (wave) domain [3,4]. With recent realizations of effective $\mathcal{PT}$ symmetry and exceptional points in minimal quantum systems, the subject of non-Hermitian quantum systems is at the forefront again. Although most studies to date have been limited to single-particle systems, non-Hermitian quantum many-particle systems are an emerging and challenging frontier. This is true because most approximate methods—variational principle, tensor networks, and perturbation theory—developed to reduce the exponential complexity of a many-body system, are designed for and work only with Hermitian Hamiltonians.

The task of simulating non-Hermitian, quantum many-particle systems, including noninteracting bosons propagating with a non-Hermitian Hamiltonian, brings new challenges [49,50]. We have shown that a programmable, unitary simulator is suited to addressing these challenges. Combined with the increasing sophistication of integrated photonic
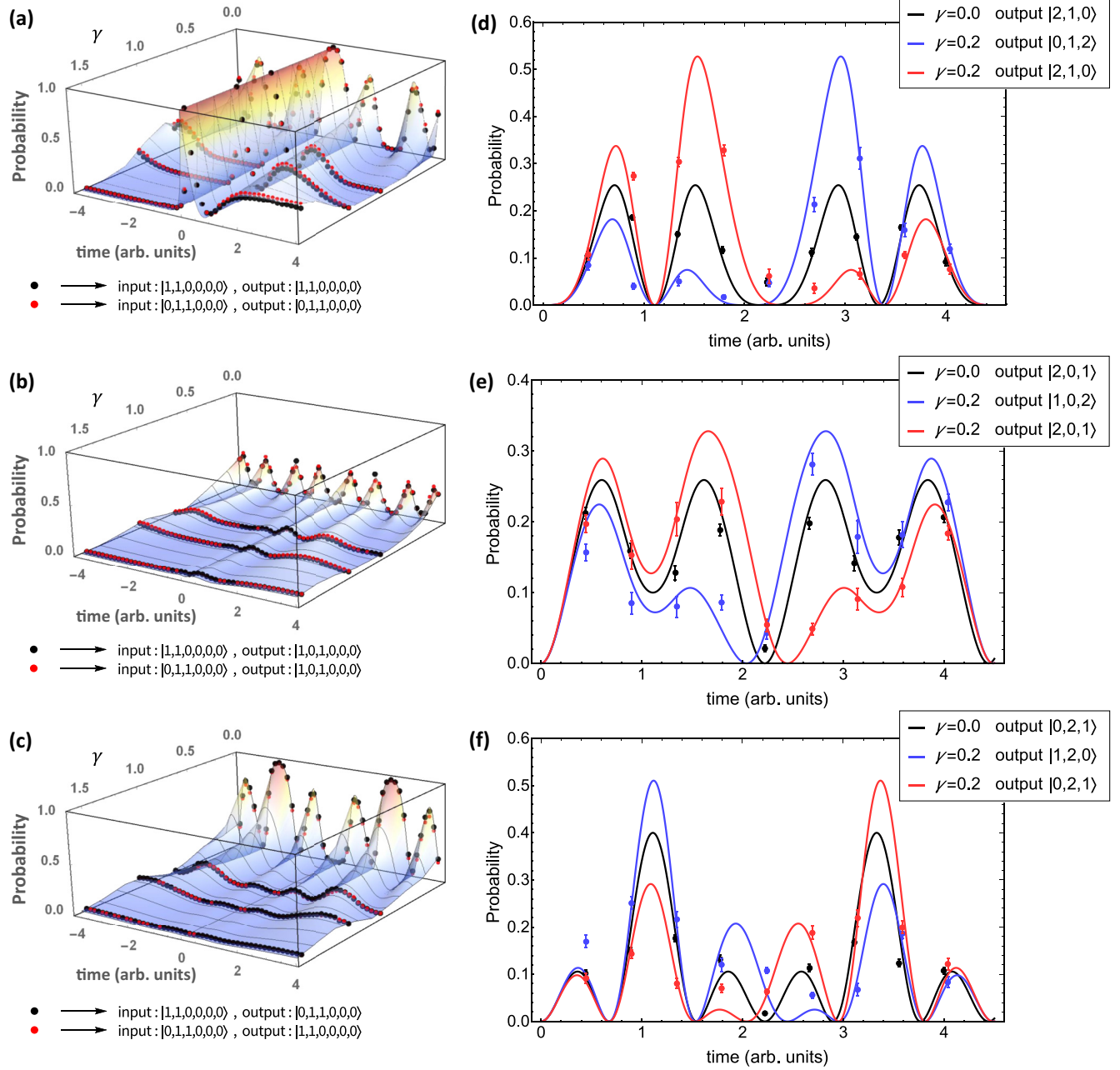
FIG. 4. (a)–(c) Two-photon correlation measurements. Data representing the evolution of the input states $|\Omega_1\rangle = |1_p 1_p 0_p\rangle_F \otimes |0_p 0_p 0_p\rangle_R$ and $|\Omega_2\rangle = |0_p 1_p 1_p\rangle_F \otimes |0_p 0_p 0_p\rangle_R$. The plot shows the probabilities of detecting the output patterns $|1_p 1_p 0_p\rangle_F \otimes |0_p 0_p 0_p\rangle_R$, $|1_p 0_p 1_p\rangle_F \otimes |0_p 0_p 0_p\rangle_R$, and $|0_p 1_p 1_p\rangle_F \otimes |0_p 0_p 0_p\rangle_R$, with dots corresponding to experimental data. Data collected for the state $|\Omega_2\rangle$ (in red) are plotted in the reverse temporal direction. Data for input state $|\Omega_2\rangle$ follow the same evolution as for input state $|\Omega_1\rangle$, provided that the output patterns $|1_p 0_p 0_p\rangle_F$ and $|0_p 1_p 1_p\rangle_F$ are exchanged. (d)–(f) Three-particle evolution. When $\gamma > 0$, the output patterns related by a spatial inversion symmetry evolve in opposite directions in time. The curves for these related output patterns become identical when $\gamma = 0$. Error bars are obtained via bootstrapping methods [45].

devices, our simulation techniques will allow the investigation of $\mathcal{PT}$-symmetric quantum systems beyond the computational capability of classical computers, paving the way for quantum technologies that can simulate and harness the potential advantages of non-Hermitian quantum systems.

APPENDIX A: UNITARY DILATION PROCEDURE

To dilate a nonunitary operator $G_N(t)$ of size $N \times N$, we must first ensure that its maximum singular value is less than

1, $\|G(t)\|_2 \leqslant 1$. We enforce this condition by scaling the operator $G_N(t)$ by a multiplicative factor α. Such normalization does not alter the quantity of the form

$$\frac{\text{Tr}[\Pi \alpha G(\gamma,t) \rho G^\dagger(\gamma,t) \alpha^*]}{\text{Tr}[\alpha G(\gamma,t) \rho G^\dagger(\gamma,t) \alpha^*]} = \frac{|\alpha|^2}{|\alpha|^2} \frac{\text{Tr}[\Pi G(\gamma,t) \rho G^\dagger(\gamma,t)]}{\text{Tr}[G(\gamma,t) \rho G^\dagger(\gamma,t)]},$$

where Π is a linear operator. Therefore α does not affect the resulting statistics of our simulations. We can either choose the scaling factor to be the maximum singular value over both time and spectrum of singular values or choose to use a time-varying scaling factor that is the maximum over the spectrum of singular values at time t. That is, $G_N(t)$ is normalized as

$$\tilde{G}_N(t) = \frac{G_N(t)}{\max_t [\|G_N(t)\|_2]} \quad \text{or} \quad \tilde{G}_N(t) = \frac{G_N(t)}{\|G_N(t)\|_2}. \tag{A1}$$

The second solution was preferred since it better adapts to the broken symmetry regime cases where the singular value of $G_N(t)$ increases exponentially with time. $\tilde{G}_N(t)$ can be decomposed by singular value decomposition as $U \cos \overrightarrow{\theta} V^\dagger$, where U, V are N-dimensional unitary matrices and $\cos \overrightarrow{\theta} = \text{diag}(\cos \theta_1, \ldots, \cos \theta_N)$. This allows for $\tilde{G}_N(t)$ to be embedded in the upper left corner of a $2N \times 2N$ unitary matrix. Indeed, possible dilations of $\tilde{G}_N(t)$ can be written as

$$U_{2N}(\gamma,t) = \begin{pmatrix} U & 0 \\ 0 & A \end{pmatrix} \begin{pmatrix} \cos \overrightarrow{\theta} & i \sin \overrightarrow{\theta} \\ i \sin \overrightarrow{\theta} & \cos \overrightarrow{\theta} \end{pmatrix} \begin{pmatrix} V^\dagger & 0 \\ 0 & B \end{pmatrix} \tag{A2}$$

for any N-dimensional unitary matrix A and B and for $\sin \overrightarrow{\theta} = \text{diag}(\sqrt{1 - \cos \theta_1^2}, \ldots, \sqrt{1 - \cos \theta_N^2})$. Setting $A = V$ and $B = U^\dagger$ gives

$$U_{2N}(\gamma,t) = \begin{pmatrix} U \cos \overrightarrow{\theta} V^\dagger & iU \sqrt{I - \cos^2 \overrightarrow{\theta}} U^\dagger \\ iV \sqrt{I - \cos^2 \overrightarrow{\theta}} V^\dagger & V \cos \overrightarrow{\theta} U^\dagger \end{pmatrix}. \tag{A3}$$

Furthermore, if C is a semipositive definite diagonal matrix, by using that for a unitary matrix W and a matrix $E = WCW^\dagger$, $\sqrt{E} = W\sqrt{C}W^\dagger$, we obtain

$$U_{2N}(\gamma,t) = \begin{pmatrix} \tilde{G}_N(t) & i\sqrt{I - \tilde{G}_N(t)\tilde{G}_N^\dagger(t)} \\ i\sqrt{I - \tilde{G}_N^\dagger(t)\tilde{G}_N(t)} & \tilde{G}_N^\dagger(t) \end{pmatrix}. \tag{A4}$$

Since in our model $G_N(t) = G_N^{\text{T}}(t)$, we have $V = U^*$ and $(\sqrt{I - \tilde{G}_N^\dagger(t)\tilde{G}_N(t)})^* = \sqrt{I - \tilde{G}_N(t)\tilde{G}_N^\dagger(t)}$. Then, defining the defect operator as $D_N(t) = \sqrt{I - \tilde{G}_N(t)\tilde{G}_N^\dagger(t)}$, we can rewrite U_{2N} as

$$U_{2N}(\gamma,t) = \begin{pmatrix} \tilde{G}_N(t) & iD_N(t) \\ iD_N^*(t) & \tilde{G}_N^\dagger(t) \end{pmatrix}. \tag{A5}$$

In the case when H_N is Hermitian, $G_N(t)$ is unitary and the singular values are 1, so $D_N = 0$, giving two independently evolving systems.

APPENDIX B: EFFECTIVE HAMILTONIAN

As the evolution of the pair of coupled systems is unitary, it can be generated by a Hermitian Hamiltonian H_{eff} over the $2N$ modes satisfying the equation

$$H_{\text{eff}} U_{2N} = i \frac{d}{dt} U_{2N}. \tag{B1}$$

From this, knowing U_{2N}, it is possible to obtain $H_{\text{eff}} = i(\frac{d}{dt} U_{2N}) U_{2N}^\dagger$ and numerically solve for H_{eff}, which turns out to be time dependent. In Fig. 5 we show the results of the numerical calculation of the H_{eff} elements for $N = 2$ and $\gamma \in \{0.25, 0.9, 1.1\}$. In the symmetric regime, the elements oscillate with a recurrence time $\tau = 2\pi/\sqrt{1 - \gamma^2}$, so

we set an equivalent "relaxation time" $\tau = 2\pi/\sqrt{|1 - \gamma^2|}$ in the broken regime. The unplotted elements in Fig. 5 are all (numerically) 0 including all diagonal elements $H_{k,k}$ for $1 \leqslant k \geqslant 4$. The spikes appearing in $H_{1,3}$ and $H_{2,4}$ represent asymptotes.

APPENDIX C: FORWARD AND REVERSE SYSTEMS WITH VACUUM CONTRIBUTION

The dynamics of the forward (F) and reverse (R) systems are recovered by the reduced states of the full $2N$-mode system:

$$\rho_{\text{F}}(t) = \text{Tr}_{\text{R}} \rho(t) := \text{Tr}_{\text{R}}[\mathcal{U}_{2N}(\gamma,t) \rho(0) \mathcal{U}_{2N}^\dagger(\gamma,t)],$$

$$\rho_{\text{R}}(t) = \text{Tr}_{\text{F}} \rho(t) := \text{Tr}_{\text{F}}[\mathcal{U}_{2N}(\gamma,t) \rho(0) \mathcal{U}_{2N}^\dagger(\gamma,t)]. \tag{C1}$$

Here, $\rho(0)$ is the input photonic state, and $\mathcal{U}_{2N}$ is the unitary operator acting on the photonic Fock space according to the transfer matrix $U_{2N}(\gamma,t)$, which transforms the input-mode creation operators $a_i^\dagger$ as

$$\mathcal{U}_{2N}(\gamma,t) a_i^\dagger \mathcal{U}_{2N}^\dagger(\gamma,t) = \sum_j [U_{2N}(\gamma,t)]_{ji} a_j^\dagger. \tag{C2}$$

To simulate a single N-dimensional $\mathcal{PT}$ system, we use $2N$ optical modes, and we assume that the optical system is
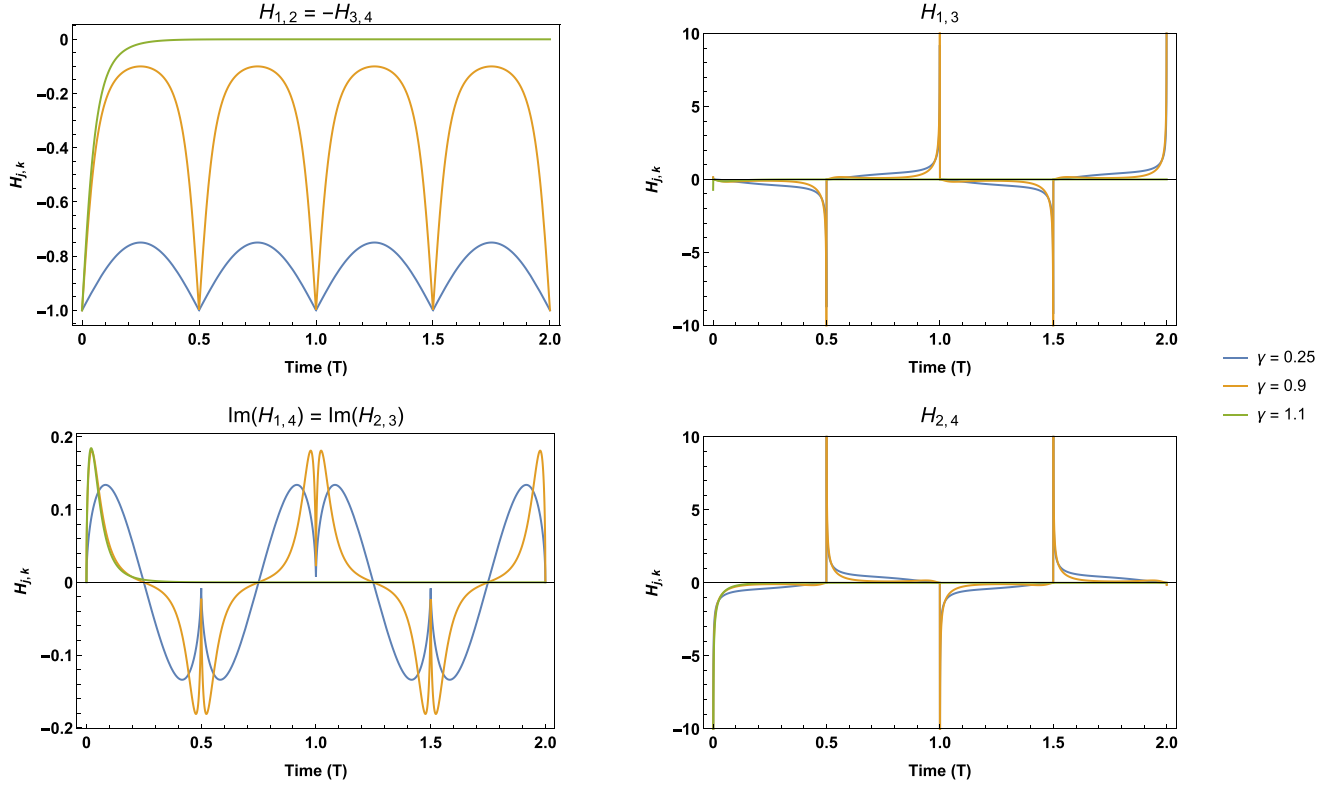
FIG. 5. Nonzero elements of the effective Hamiltonian H_{eff} of the dilated unitary for the two-mode $\mathcal{PT}$-symmetric Hamiltonian H_2.

constrained to the one-photon subspace. In this space a basis is

$$\{|k\rangle = |0_p\rangle^{\otimes(k-1)}|1_p\rangle|0_p\rangle^{\otimes(2N-k)}\}_{k=1}^{2N}, \qquad (C3)$$

where $|0_p\rangle$ is the single-mode vacuum state. Doing this, the density matrix at time t can then be denoted as

$$\rho(t) = U_{2N}(\gamma, t)\rho(0)U_{2N}^{\dagger}(\gamma, t). \qquad (C4)$$

However, we can treat the modes 1 to N as composing the forward system and modes from $N+1$ to $2N$ as composing the reverse system leading to the definition of two reduced density matrices obtained performing the partial trace over one of the systems. For the reduced density matrix of the forward system ρ_F we obtain

$$\begin{aligned}
\rho_F = \mathrm{tr}_R\rho &= \mathrm{tr}_R \sum_{k,l=1}^{2N} p_{kl}|k\rangle\langle l| \\
&= \mathrm{tr}_R \sum_{k,l=1}^{2N} p_{kl}|0_p\rangle^{\otimes(k-1)}|1_p\rangle|0_p\rangle^{\otimes(2N-k)}\langle 0_p|^{\otimes(l-1)}\langle 1_p|\langle 0_p|^{\otimes(2N-l)} \\
&= \mathrm{tr}_R\Bigg(\sum_{k,l=1}^{N} p_{kl}|0_p\rangle^{\otimes(k-1)}|1_p\rangle|0_p\rangle^{\otimes(2N-k)}\langle 0_p|^{\otimes(l-1)}\langle 1_p|\langle 0_p|^{\otimes(2N-l)} \\
&\quad + \sum_{k,l=N+1}^{2N} p_{kl}|0_p\rangle^{\otimes(k-1)}|1_p\rangle|0_p\rangle^{\otimes(2N-k)}\langle 0_p|^{\otimes(l-1)}\langle 1_p|\langle 0_p|^{\otimes(2N-l)} \\
&\quad + \sum_{k=1}^{N}\sum_{l=N+1}^{2N} p_{kl}|0_p\rangle^{\otimes(k-1)}|1_p\rangle|0_p\rangle^{\otimes(2N-k)}\langle 0_p|^{\otimes(l-1)}\langle 1_p|\langle 0_p|^{\otimes(2N-l)} \\
&\quad + \sum_{k=N+1}^{2N}\sum_{l=1}^{N} p_{kl}|0_p\rangle^{\otimes(k-1)}|1_p\rangle|0_p\rangle^{\otimes(2N-k)}\langle 0_p|^{\otimes(l-1)}\langle 1_p|\langle 0_p|^{\otimes(2N-l)} \Bigg)
\end{aligned}$$

$$= \sum_{k,l=1}^{N} p_{kl} |0_p\rangle^{\otimes(k-1)} |1_p\rangle |0_p\rangle^{\otimes(N-k)} \langle 0_p|^{\otimes(l-1)} \langle 1_p| \langle 0_p|^{\otimes(N-l)} + \sum_{k,l=N+1}^{2N} p_{kl} |0_p\rangle^{\otimes N} \langle 0_p|^{\otimes N} \delta_{k,l}$$

$$= \sum_{k,l=1}^{N} p_{kl} |k\rangle \langle l| + \sum_{k=N+1}^{2N} p_{kk} |\text{vac}\rangle \langle \text{vac}|.$$

Similar results are obtained when the partial trace is performed over the forward system, showing that the partial trace operation over the reverse (forward) system sums the diagonal elements of the bottom (top) N modes of $\rho(t)$ and places this value in the vacuum state of the forward (reverse) system. That is, the Fock spaces of the systems are decomposed into particle number subspaces as $\mathcal{F}^{(F/R)} = \mathcal{H}_0^{(F/R)} \oplus \mathcal{H}_1^{(F/R)}$. According to this, we can choose the basis states of the forward or reverse system as $\{|k\rangle^{(F/R)} = |0_p\rangle^{\otimes(k-1)} |1_p\rangle |0_p\rangle^{\otimes(N-k)}\}_{k=1}^{N}$ and an additional basis state in each system $|\text{vac}\rangle = |0_p\rangle^{\otimes N}$. Furthermore, no coherence is present between the one-photon and zero-photon subspaces.

Whenever there is interest in considering only the original $\mathcal{PT}$ system without introducing the reverse system and the interaction terms between them, we need to redefine the density matrix of the forward system without including the vacuum contribution as

$$\tilde{\rho}_F = \frac{\sum_{k,l=1}^{N} p_{kl} |k\rangle \langle l|}{\sum_{k=1}^{N} p_{kk}}. \tag{C5}$$

This approach has been used in the simulation of the no-signaling violation.

APPENDIX D: EXPERIMENTAL METHODS

1. Photon generation

For all the experiments described in this paper, the single photons are generated via spontaneous parametric downconversion in a bismuth borate nonlinear crystal satisfying type I phase-matching conditions. The crystal is pumped with light pulses at 404 nm obtained from a second-harmonic-generation process induced in a barium borate crystal by a 808-nm Ti:sapphire mode-locked laser. The pairs of photons generated in the downconversion are spectrally filtered with a 3-nm-bandwidth interferometric filter centered around 808 nm and are collected from two diametrically opposite positions of the generation cone. The pair of photons, coupled to single-mode polarization-maintaining fibers, are used either as a two-photon Fock state, by injecting them both into our interferometer, or as a heralded single photon by connecting one of the two fibers to a single-photon detector and injecting the other photon into the interferometer. When interested in the two-photon Fock state, we record all the events where two single photons are detected at the output of the chip. For the experiments in which we only need a single photon source, we record all the events when both the heralding photon and the photon at the output of the chip are detected. Three-photon experiments are performed collecting two separate pairs of photons from the emission cone and recording the coincidental detection of a heralding photon from one pair and

of three photons passing through the optical modes of the interferometer.

2. Integrated interferometer

The programmable interferometer used to implement the multiple unitary transfer matrices of the experiments was produced by the NTT Group in Japan and is described in Ref. [27]. The triangular arrangement of 15 integrated Mach-Zehnder interferometers with 30 thermally tunable phase shifters allows us to prepare any unitary optical transfer matrix across six modes. Alternatively, the same device can be used as a cascade of 2×2 interferometers in order to sequentially implement state preparation, evolution, or projection in physically different parts of the chip.

3. Probabilistic number resolving

The three-photon simulations reported in this paper require the ability to resolve multiple occupancy in the output modes to detect bunching photon events. To measure the probability of these events, we performed probabilistic number resolving detection of up to two photons in the same mode using auxiliary fiber beam splitters (FBSs) and detectors. By inserting a FBS at each of the first three output modes of the interferometer and connecting both output modes of each FBS to detectors, there is a finite probability that photons bunched in the same output mode separate at the FBS and generate a signal at both detectors to which the FBS is connected.

4. Detection calibration

We experimentally estimate the probability of collapsing the quantum state of our simulator onto a particular Fock state by multiplying the number of occurrences of each detected pattern by a detector calibration factor associated with that pattern and then normalizing to unity the sum over all relevant output patterns. The relative detector efficiency at the different output modes, for single-photon events, is obtained by testing 500 random phase configurations of our interferometer and comparing the experimental statistic with the expected photon statistics due to the phase settings. The efficiency correction of each mode that maximizes the statistical fidelity between the experimental statistics and the theoretical distribution is chosen as a numerical correction for the data collected during single-photon experiments. For two-photon antibunched events, the occurrence of each pattern is multiplied by the product of the correction factor of the individual output modes populated with photons.

In the pseudo-number-resolving configuration, the detection calibration factor is obtained by using the single-photon detector efficiency ν_i recorded at each output of the FBS.
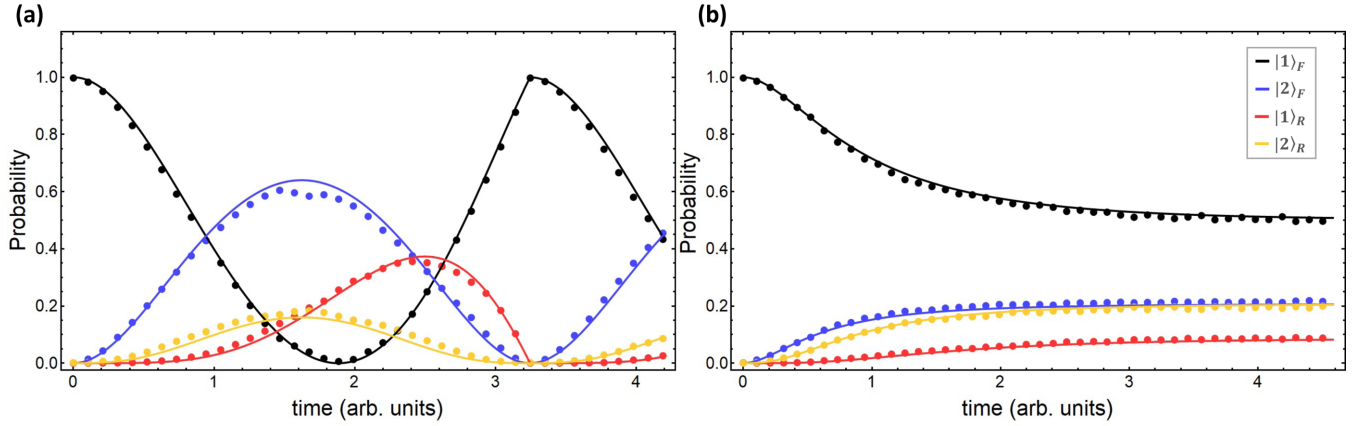
FIG. 6. Plots showing the evolution of a single excitation in the forward subsystem. Solid lines (points) show the theoretical curve (experimental data). We show the probabilities for the excitation being detected in the forward subsystem ($|1\rangle_F$, $|2\rangle_F$) and the reverse subsystem ($|1\rangle_R$, $|2\rangle_R$). Both panels follow the legend in (b). (a) Plots for a $\mathcal{PT}$ Hamiltonian in the unbroken regime ($\gamma = 0.25$). We see periodic oscillations of the excitation in all four modes. (b) Plots for the broken symmetry regime. All probabilities evolve exponentially to a steady state ($\gamma = 1.1$).

To take into account the probabilistic nature of the pseudo-number-resolving scheme, the experimental occurrence of a detection pattern such as $((n_{1,1}, n_{1,2}), (n_{2,1}, n_{2,2}), (n_{3,1}, n_{3,2}))$ is divided by

$$\Gamma((n_{1,1}, n_{1,2}), (n_{2,1}, n_{2,2}), (n_{3,1}, n_{3,2}))$$
$$= \prod_{i=1}^{i=3} \nu_{i,1}^{n_{i,1}} \nu_{i,2}^{n_{i,2}} (n_{i,1} + n_{i,2})! \quad \text{(D1)}$$

The number of events associated with an output state $|N_{1p} N_{2p} N_{3p}\rangle$ with $N_{kp} = n_{k,1} + n_{k,2}$ is given as the average of the occurrences of equivalent detection patterns. For example, $((1, 1), (1, 0), (0, 0))$ is equivalent to $((1, 1), (0, 1), (0, 0))$ since both correspond to the output state $|2_p 1_p 0_p\rangle$. The final probabilities are normalized over all the output states characterized by three photons in the forward system modes but with less than three photons bunched in the same mode.

5. State preparation and reconstruction

The preparation of fully mixed single-photon states is obtained by the interference of two indistinguishable single photons. The Hong-Ou-Mandel visibility of their interference is measured to be 0.97. During the entropy evolution simulation, the interferometer is set to implement $U_{\text{Proj}} U_4(\gamma, t) U_{\text{Ent}}$, where

$$U_{\text{Ent}} = \begin{pmatrix} 0 & 0 & \frac{\sqrt{2}}{2} & \frac{\sqrt{2}}{2} & 0 & 0 \\ 0 & 0 & 0 & 0 & \frac{\sqrt{2}}{2} & \frac{\sqrt{2}}{2} \\ 1 & 0 & 0 & 0 & 0 & 0 \\ 0 & 1 & 0 & 0 & 0 & 0 \\ 0 & 0 & \frac{\sqrt{2}}{2} & -\frac{\sqrt{2}}{2} & 0 & 0 \\ 0 & 0 & 0 & 0 & \frac{\sqrt{2}}{2} & -\frac{\sqrt{2}}{2} \end{pmatrix}, \quad \text{(D2)}$$

$U_4(\gamma, t)$ transforms the bottom four modes of the interferometer, and U_{Proj} projects the bottom two modes on the bases of the Pauli operators. Physically separate components of the optical circuit are involved in the implementation of the three cascaded unitaries. The evolution of excitations super-posed across the forward and reverse systems is performed by compiling the two transformations required for preparing and evolving the states. The resulting unitary is implemented in the first part of the chip. The expectation values of S_F and S_R are measured using three further concatenated interferometers to project each of the systems, independently, on the eigenstates of the Pauli operators.

When $N = 3$, to simulate the evolution of a single-particle state prepared in a superposition across multiple modes of the forward or reverse system, we multiplied the transfer matrix $U_6(\gamma, t)$ with the state rotation necessary to transform a localized single photon into the desired superposition. The resulting unitary transformation is then dialed on the optical chip.

The experiment with two-photon Fock states is performed setting the transfer matrix of the chip to implement $U_6(\gamma, t)$ while the input state is obtained injecting either $|0_p 1_p 1_p\rangle_F \otimes |0_p 0_p 0_p\rangle_R$ or $|1_p 1_p 0_p\rangle_F \otimes |0_p 0_p 0_p\rangle_R$ into our integrated interferometer. The production of the desired input state is assumed every time a coincidence detection happens at two of the detectors connected to the output modes of our device neglecting higher-order pair generation occurring with a two-order-of-magnitude-lower rate.

APPENDIX E: REVERSE SUBSYSTEM IN A TWO-MODE SYSTEM

In the main text we show the dynamics of an excitation in the forward subsystem for a two-mode $\mathcal{PT}$ system. We included a combined vacuum probability which contained the probability of the excitation tunneling into the reverse subsystem. Using the same experimental data, in Fig. 6 we show the evolution of both forward and both reverse modes. This captures the full dynamics of a single excitation in the forward subsystem. We show the data for both the unbroken ($\gamma = 0.25$) and broken ($\gamma = 1.1$) symmetry regimes. We see a periodic oscillation in the probability of all four modes in the unbroken regime. In the broken regime all four mode probabilities evolve exponentially towards a steady-state value.
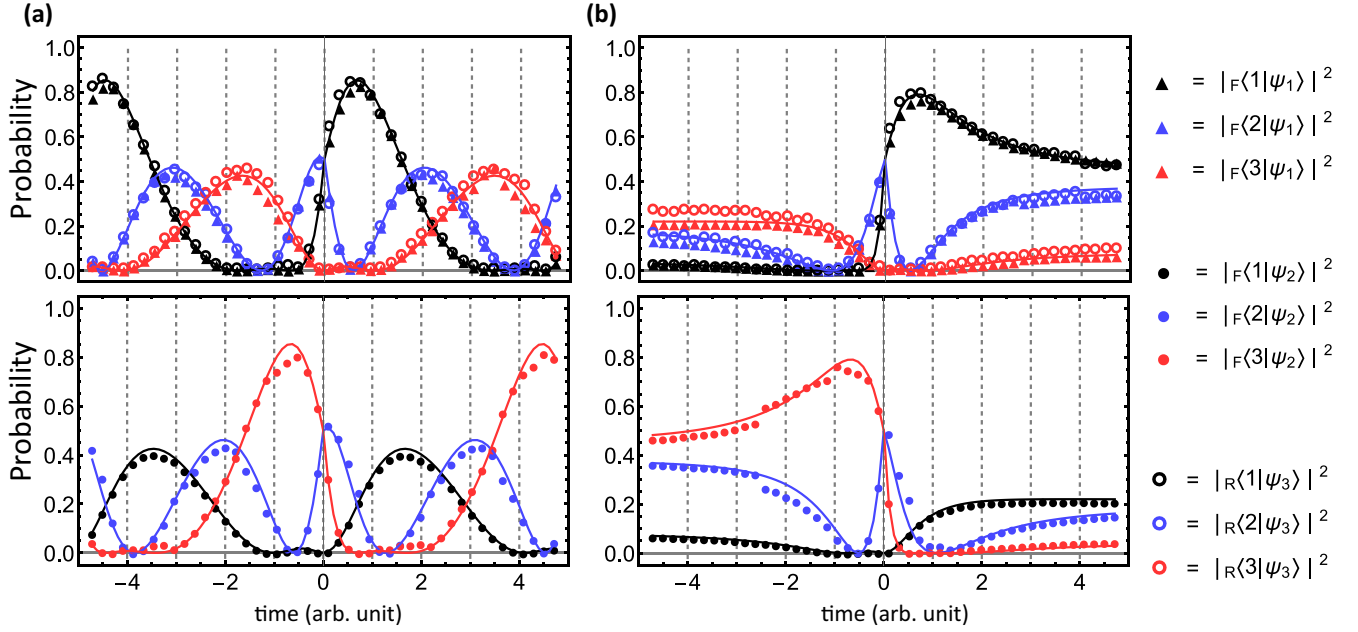
FIG. 7. Results for the simulation of the three-level $\mathcal{PT}$-symmetric Hamiltonian. Plots show the evolution of the probability, in the unbroken (a) ($\gamma = 0.5\gamma_c$) and broken (b) ($\gamma = 1.1\gamma_c$) symmetry regimes, for three input states: $|\psi_1(t=0)\rangle = (|1\rangle_F - i|2\rangle_F)/\sqrt{2}$, $|\psi_3(t=0)\rangle = (|1\rangle_R + i|2\rangle_R)/\sqrt{2}$ (top row), and $|\psi_2(t=0)\rangle = (i|2\rangle_F + |3\rangle_F)/\sqrt{2}$ (bottom row). Solid lines in the top row represent theory curves for the time evolution of $|\psi_1(t)\rangle$, while solid lines in the bottom row represent theory curves for the time evolution of $|\psi_2(t)\rangle$. The data for $|\psi_3\rangle$ show the same temporal behavior as for $|\psi_1\rangle$. Conversely, the data for $|\psi_2\rangle$ follow the opposite temporal evolution as $|\psi_1\rangle$, while the probabilities of observing $|1\rangle$ and $|3\rangle$ are exchanged.

APPENDIX F: SINGLE-PARTICLE DYNAMICS IN A THREE-MODE SYSTEM

Since, for $N = 3$, the third-order exceptional point occurs at $\gamma_c = \sqrt{2}$, to analyze unbroken and broken symmetry regimes, we perform simulations for $\gamma = \sqrt{2}/2$ and $\gamma = 1.1\sqrt{2}$, respectively. Transfer matrices, concatenating state preparation and unitary evolution described by $U_6(\gamma, t_i)$, are implemented by using the entirety of the six-mode chip.

Figure 7 shows data reproducing the evolution of three single-particle initial states $\{|\psi_1(t=0)\rangle_F, |\psi_2(t=0)\rangle_F, |\psi_3(t=0)\rangle_R\}$. These are related by symmetry transformations as follows:

$$|\psi_1(0)\rangle_F = (|1\rangle_F - i|2\rangle_F)/\sqrt{2} \tag{F1}$$

is an example of a state coherently superposed across gain and neutral sites of the forward system;

$$|\psi_2(0)\rangle_F = (i|2\rangle_F + |3\rangle_F)/\sqrt{2} = \mathcal{PT}|\psi_1(0)\rangle_F \tag{F2}$$

is the result of a $\mathcal{PT}$ transformation of $|\psi_1(0)\rangle_F$; and

$$|\psi_3(0)\rangle_R = (|1\rangle_R + i|2\rangle_R)/\sqrt{2} = \mathcal{T}|\psi_1(0)\rangle_R \tag{F3}$$

is prepared in the reverse system and, via time inversion, is analogous to the state $\mathcal{T}|\psi_1(0)\rangle_F$.

Due to the symmetries of our model, the mode occupation of these states during their evolution is closely related. Specifically, we expect

$$\langle k|\psi_2(t)\rangle = \langle k|\mathcal{PT}G_3(-t)\mathcal{PT}\psi_2(0)\rangle$$
$$= \langle 4 - k|G_3(-t)\psi_1(0)\rangle^*, \tag{F4}$$

and since $H_3(\gamma) = H_3^T(\gamma)$, we also have

$$\langle k|G_3(t)^\dagger\psi_3(0)\rangle = \langle k|\mathcal{T}G_3(t)\mathcal{T}\psi_3(0)\rangle$$
$$= \langle k|\mathcal{T}G_3(t)\psi_1(0)\rangle$$
$$= \langle k|G_3(t)\psi_1(0)\rangle^*. \tag{F5}$$

Figures 7(a) and 7(b) show that the (forward) evolution of state $|\psi_1\rangle$ with Hamiltonian H_3 is the same as the (reverse) evolution of the state $|\psi_3\rangle$ with Hamiltonian H_3^*. These results at time $-t$ match the evolution of state $|\psi_2\rangle$ with Hamiltonian H_3 at time t, demonstrating the mirror symmetry about $t = 0$.

[1] C. M. Bender, Making sense of non-Hermitian Hamiltonians, Rep. Prog. Phys. **70**, 947 (2007).

[2] A. Mostafazadeh, Pseudo-Hermitian representation of quantum mechanics, Int. J. Geom. Meth. Mod. Phys. **07**, 1191 (2010).

[3] R. El-Ganainy, K. G. Makris, M. Khajavikhan, Z. H. Musslimani, S. Rotter, and D. N. Christodoulides, Non-Hermitian physics and PT symmetry, Nat. Phys. **14**, 11 (2018).

[4] M.-A. Miri and A. Alù, Exceptional points in optics and photonics, Science **363**, eaar7709 (2019).

[5] L. Feng, Y.-L. Xu, W. S. Fegadolli, M.-H. Lu, J. E. B. Oliveira, V. R. Almeida, Y.-F. Chen, and A. Scherer, Experimental demonstration of a unidirectional reflectionless parity-time metamaterial at optical frequencies, Nat. Mater. **12**, 108 (2012).

[6] L. Feng, Z. J. Wong, R.-M. Ma, Y. Wang, and X. Zhang, Single-mode laser by parity-time symmetry breaking, Science **346**, 972 (2014).

[7] H. Hodaei, M.-A. Miri, M. Heinrich, D. N. Christodoulides, and M. Khajavikhan, Parity-time-symmetric microring lasers, Science **346**, 975 (2014).

[8] G. Harari, M. A. Bandres, Y. Lumer, M. C. Rechtsman, Y. D. Chong, M. Khajavikhan, D. N. Christodoulides, and M. Segev, Topological insulator laser: Theory, Science **359**, eaar4003 (2018).

[9] M. A. Bandres, S. Wittek, G. Harari, M. Parto, J. Ren, M. Segev, D. N. Christodoulides, and M. Khajavikhan, Topological insulator laser: Experiments, Science **359**, eaar4005 (2018).

[10] H. Xu, D. Mason, L. Jiang, and J. G. E. Harris, Topological energy transfer in an optomechanical system with exceptional points, Nature (London) **537**, 80 (2016).

[11] J. Doppler, A. A. Mailybaev, J. Böhm, U. Kuhl, A. Girschik, F. Libisch, T. J. Milburn, P. Rabl, N. Moiseyev, and S. Rotter, Dynamically encircling an exceptional point for asymmetric mode switching, Nature (London) **537**, 76 (2016).

[12] Y.-H. Lai, Y.-K. Lu, M.-G. Suh, Z. Yuan, and K. Vahala, Observation of the exceptional-point-enhanced Sagnac effect, Nature (London) **576**, 65 (2019).

[13] M. P. Hokmabadi, A. Schumer, D. N. Christodoulides, and M. Khajavikhan, Non-Hermitian ring laser gyroscopes with enhanced Sagnac sensitivity, Nature (London) **576**, 70 (2019).

[14] H. Wang, Y.-H. Lai, Z. Yuan, M.-G. Suh, and K. Vahala, Petermann-factor sensitivity limit near an exceptional point in a Brillouin ring laser gyroscope, Nat. Commun. **11**, 1610 (2020).

[15] J. Wiersig, Prospects and fundamental limits in exceptional point-based sensing, Nat. Commun. **11**, 2454 (2020).

[16] S. Scheel and A. Szameit, $\mathcal{PT}$-symmetric photonic quantum systems with gain and loss do not exist, EPL (Europhys. Lett.) **122**, 34001 (2018).

[17] L. Xiao, X. Zhan, Z. H. Bian, K. K. Wang, X. Zhang, X. P. Wang, J. Li, K. Mochizuki, D. Kim, N. Kawakami, W. Yi, H. Obuse, B. C. Sanders, and P. Xue, Observation of topological edge states in parity-time-symmetric quantum walks, Nat. Phys. **13**, 1117 (2017).

[18] J. Li, A. K. Harter, J. Liu, L. de Melo, Y. N. Joglekar, and L. Luo, Observation of parity-time symmetry breaking transitions in a dissipative Floquet system of ultracold atoms, Nat. Commun. **10**, 855 (2019).

[19] M. Naghiloo, M. Abbasi, Y. N. Joglekar, and K. W. Murch, Quantum state tomography across the exceptional point in a single dissipative qubit, Nat. Phys. **15**, 1232 (2019).

[20] U. Günther and B. F. Samsonov, Naimark-Dilated $\mathcal{PT}$-Symmetric Brachistochrone, Phys. Rev. Lett. **101**, 230404 (2008).

[21] L. Xiao, K. Wang, X. Zhan, Z. Bian, K. Kawabata, M. Ueda, W. Yi, and P. Xue, Observation of Critical Phenomena in Parity-Time-Symmetric Quantum Dynamics, Phys. Rev. Lett. **123**, 230401 (2019).

[22] Y. Wu, W. Liu, J. Geng, X. Song, X. Ye, C.-K. Duan, X. Rong, and J. Du, Observation of parity-time symmetry breaking in a single-spin system, Science **364**, 878 (2018).

[23] H.-K. Lau and D. F. V. James, Proposal for a scalable universal bosonic simulator using individually trapped ions, Phys. Rev. A **85**, 062329 (2012).

[24] C. Shen, Z. Zhang, and L.-M. Duan, Scalable Implementation of Boson Sampling with Trapped Ions, Phys. Rev. Lett. **112**, 050504 (2014).

[25] X. Gu, A. F. Kockum, A. Miranowicz, Y.-x. Liu, and F. Nori, Microwave photonics with superconducting quantum circuits, Phys. Rep. **718**, 1 (2017).

[26] F. Klauck, L. Teuber, M. Ornigotti, M. Heinrich, S. Scheel, and A. Szameit, Observation of $\mathcal{PT}$-symmetric quantum interference, Nat. Photonics **13**, 883 (2019).

[27] J. Carolan, C. Harrold, C. Sparrow, E. Martín-López, N. J. Russell, J. W. Silverstone, P. J. Shadbolt, N. Matsuda, M. Oguma, M. Itoh, G. D. Marshall, M. G. Thompson, J. C. F. Matthews, T. Hashimoto, J. L. O'Brien, and A. Laing, Universal linear optics, Science **349**, 711 (2015).

[28] L. Jin and Z. Song, Solutions of $\mathcal{PT}$-symmetric tight-binding chain and its equivalent Hermitian counterpart, Phys. Rev. A **80**, 052107 (2009).

[29] Y. N. Joglekar, D. Scott, M. Babbey, and A. Saxena, Robust and fragile $\mathcal{PT}$-symmetric phases in a tight-binding chain, Phys. Rev. A **82**, 030103(R) (2010).

[30] P. R. Halmos, Normal dilations and extensions of operators, Summa Bras. Math. **2**, 125 (1950).

[31] K. Wang, Y. Shi, L. Xiao, J. Wang, Y. N. Joglekar, and P. Xue, Experimental realization of continuous-time quantum walks on directed graphs and their application in PageRank, Optica **7**, 1524 (2020).

[32] C. Sparrow, E. Martín-López, N. Maraviglia, A. Neville, C. Harrold, J. Carolan, Y. N. Joglekar, T. Hashimoto, N. Matsuda, J. L. O'Brien, D. P. Tew, and A. Laing, Simulating the vibrational quantum dynamics of molecules using photonics, Nature (London) **557**, 660 (2018).

[33] P. Peng, W. Cao, C. Shen, W. Qu, J. Wen, L. Jiang, and Y. Xiao, Anti-parity–time symmetry with flying atoms, Nat. Phys. **12**, 1139 (2016).

[34] M. Reck, A. Zeilinger, H. J. Bernstein, and P. Bertani, Experimental Realization of Any Discrete Unitary Operator, Phys. Rev. Lett. **73**, 58 (1994).

[35] Z. Y. Ou and L. Mandel, Violation of Bell's Inequality and Classical Probability in a Two-Photon Correlation Experiment, Phys. Rev. Lett. **61**, 50 (1988).

[36] K. Kawabata, Y. Ashida, and M. Ueda, Information Retrieval and Criticality in Parity-Time-Symmetric Systems, Phys. Rev. Lett. **119**, 190401 (2017).

[37] Y. C. Lee, M. H. Hsieh, S. T. Flammia, and R. K. Lee, Local $\mathcal{PT}$ Symmetry Violates the No-Signaling Principle, Phys. Rev. Lett. **112**, 130404 (2014).

[38] J. Tang, Y. Wang, S. Yu, D. He, J. Xu, B. Liu, G. Chen, Y. Sun, K. Sun, Y. Han, C. Li, and G. Guo, Experimental investigation of the no-signalling principle in parity-time symmetric theory using an open quantum system, Nat. Photonics **10**, 642 (2016).

[39] Y. Aharonov and L. Susskind, Charge superselection rule, Phys. Rev. **155**, 1428 (1967).

[40] E. Schrödinger, Über die kräftefreie Bewegung in der relativistischen Quantenmechanik, Sitzungber. Preuss. Akad. Wiss. Phys.-Math. Kl. **24**, 418 (1930).

[41] O. Klein, Die Reflexion von Elektronen an einem Potentialsprung nach der relativistischen Dynamik von Dirac, Z. Phys. **53**, 157 (1929).

[42] L. J. LeBlanc, M. C. Beeler, K. Jiménez-García, A. R. Perry, S. Sugawa, R. A. Williams, and I. B. Spielman, Direct observation of zitterbewegung in a Bose-Einstein condensate, New J. Phys. **15**, 073011 (2013).

[43] R. Gerritsma, G. Kirchmair, F. Zähringer, E. Solano, R. Blatt, and C. Roos, Quantum simulation of the Dirac equation, Nature (London) **463**, 68 (2010).

[44] For continuous-variable systems, the coordinate operator is defined as $\hat{x} = (\hat{a}^{\dagger} + \hat{a})/\sqrt{2}$, where $\hat{a}^{\dagger}$ and $\hat{a}$ are the particle creation and annihilation operators. In turn, for discrete-variable systems, one can write down the Pauli $\hat{\sigma}^x$ matrix as $\hat{\sigma}^x = (\hat{S}^+ + \hat{S}^-)/\sqrt{2}$, where $\hat{S}^{\pm}$ are Pauli ladder operators. Since the creation and annihilation operators are similar to ladder operators in their action in the state space, in this context, we consider $\hat{\sigma}^x$ as the discrete-variable analog of $\hat{x}$.

[45] G. Simpson and H. Mayer-Hasselwander, Bootstrap sampling: applications in gamma-ray astronomy, Astron. Astrophys. **162**, 340 (1986).

[46] S. Aaronson and A. Arkhipov, The computational complexity of linear optics, Theory Comput. **9**, 143 (2013).

[47] J. J. Renema, V. Shchesnovich, and R. Garcia-Patron, Boson sampling with linear loss is classically simulable, in *Quantum Information and Measurement (QIM) V: Quantum Technologies* (Optical Society of America, Washington, DC, 2019), p. F3A.3.

[48] C. M. Bender, D. C. Brody, and H. F. Jones, Complex Extension of Quantum Mechanics, Phys. Rev. Lett. **89**, 270401 (2002).

[49] Y. Ashida, S. Furukawa, and M. Ueda, Parity-time-symmetric quantum critical phenomena, Nat. Commun. **8**, 15791 (2017).

[50] B. Dóra and C. P. Moca, Quantum Quench in $\mathcal{PT}$-Symmetric Luttinger Liquid, Phys. Rev. Lett. **124**, 136802 (2020).